TTP92–28
September 1992

HEAVY QUARK PRODUCTION AT A PHOTON LINEAR COLLIDER

J. H. Kühn, E. Mirkes and J. Steegborn

Institut für Theoretische Teilchenphysik
Universität Karlsruhe
Kaiserstr. 12, Postfach 6980
7500 Karlsruhe 1, Germany

Abstract

Heavy quark production at future Compton colliders is investigated. The impact of polarization has been studied. Perturbative QCD corrections to the effective cross section are calculated and found to be at the level of 40% for a e^+e^- collider of 500 GeV and a top quark mass of 150 GeV. The η_t resonance structure is incorporated.

1 Introduction

The search for the elusive top quark, the determination of its mass and the study of its electroweak couplings constitutes an important part of the program of presently operating accelerators and of those of the next generation. Top quark production in hadronic collisions and in electron positron annihilation (For a recent reviev see e.g. [1]) has been discussed quite frequently in the literature and will certainly be in the forefront of these studies. In addition there is the option for high energy photon-photon collisions at a future "Compton collider". Such an experiment would make use of well focussed high energy photons produced through backscattering of laser light from high energy electron beams. Production of Higgs bosons [2] or of W pairs [3] in photon photon fusion are reactions of great interest, t-$\bar{t}$–production is also possible with large rates and could provide interesting information on the top-photon coupling.

The production cross section of top quarks depends sensitively on the initial photon polarization. In section 2 of this paper analytical formulae are derived for the γ-γ–luminosity as a function of the γ-γ–energy and of the initial electron and the laser polarization and decomposed according to the energetic photon helicities. In section 3 the Born cross section for $\gamma\gamma \to t\bar{t}$ will be folded with these luminosities leading to a substantial effective cross section e.g. for a e^+e^- collider of 500 GeV. Strong dependence of the production rate on laser and electron polarization is observed[1].

Only "direct" photon induced amplitudes will be considered. Contributions from the hadronic component of the photon are small. This is a consequence of the steeply falling quark and gluon distribution in the photon and the fact that $4m_t^2/s_{\gamma\gamma}$ is of order one. QCD corrections to top quark production are evaluated in section 4 and found to be large – in particular in the threshold region. For the approximate choice of α_s a smooth matching between continuum region and resonances is observed, which allows to evaluate again an effective cross section by folding the QCD corrected $\gamma\gamma \to t\bar{t}$ cross section with the luminosity spectrum derived in section 2. Large corrections are observed also after this convolution.

2 Differential $\gamma\gamma$-luminosities

There are copious ways that can lead to photon-photon collisions at an e^+e^- collider. Apart from collisions of slightly virtual photons, beamstrahlung and Compton scattering are the most promising sources [5]. Backscattering a laser beam off energetic electrons offers an efficient mechanism to convert electrons

[1]These results in Born approximation have been presented in a preliminary version in [4]

into photons and reach thus the highest possible photon-photon luminosity and energy [6, 7, 8, 2]. In the following we shall concentrate on photons from this source. Reactions induced by beamstrahlung will typically arise from lower energy photons and hence can easily be distinguished from $t\bar{t}$ production with its large $s_{\gamma\gamma}$ required to cross the top quark threshold. The compton cross section σ_c depends on the initial and final state polarization [9]. For collinear electron and laser beams the differential cross section is given by

$$\frac{d\sigma_c}{dy} = \frac{\pi\alpha^2}{xm_e^2}\left[f_0 + P_e P_\gamma f_1 + P_e P_{\gamma'} f_2 + P_\gamma P_{\gamma'} f_3\right] \tag{1}$$

$$f_0 = \frac{1}{1-y} + 1 - y - 4r(1-r) \qquad\qquad f_1 = xr(1-2r)(2-y)$$

$$f_2 = xr\left(1 + (1-y)(1-2r)^2\right) \qquad\qquad f_3 = (1-2r)\left(\frac{1}{1-y} + 1 - y\right)$$

$$x = \frac{4E\omega_0}{m_e^2} \qquad\qquad y = 1 - \frac{pk}{pk_0} \approx \frac{\omega}{E} \qquad\qquad r = \frac{y}{x(1-y)}$$

$$0 \le y \le y_{max} = \frac{x}{x+1}$$

with E, ω_0 and ω as the energies of the incoming electron and photon and of the final state photon in the laboratory frame respectively. P_e, P_γ and $P_{\gamma'}$ denote the helicities of the initial electron, laser and scattered photon with $-1 \le P_e, P_\gamma, P_{\gamma'} \le +1$. For backscattering y denotes the fraction of electron energy transfered to the photon. In the case of opposite helicities of electron and laser the spectrum $\frac{dN}{dy} = \frac{1}{\sigma_c}\frac{d\sigma_c}{dy}$ is peaked at high energies and depleted in the medium energy range (Fig. 1). Full (or vanishing) longitudinal polarization both for electrons and incoming photons is assumed and, if not stated otherwise, an electron energy E $= 250$ GeV and a laser energy $\omega_0 = 1.26$ eV. These values imply $x \approx 4.83$ close below the threshold for the undesirable production of an e^+e^- pair in the collision of a high energy and a laser photon [8, 10]. Choosing equal helicities of incoming electrons and photons enhances the spectrum for intermediate energies with a corresponding depletion towards the high end. The spectrum is decomposed according to the helicities of the backscattered photon in Fig. 2. For high energies the helicity flip contribution dominates, below $y \approx 0.55$ the helicity conserving part is more important. These photon energy distributions allow to calculate normalized spectral $\gamma\gamma$-luminosities $\frac{dL}{dz}$ through[2] [9]

$$\frac{dL}{dz} = 2z \int\limits_{z^2/y_{max}}^{y_{max}} \frac{dy}{y}\left(\frac{1}{\sigma_c}\frac{d\sigma_c(y)}{dy}\right)\left(\frac{1}{\tilde{\sigma}_c}\frac{d\tilde{\sigma}_c(z^2/y)}{d(z^2/y)}\right) \tag{2}$$

[2]The tilde denotes quantities related to the second beam

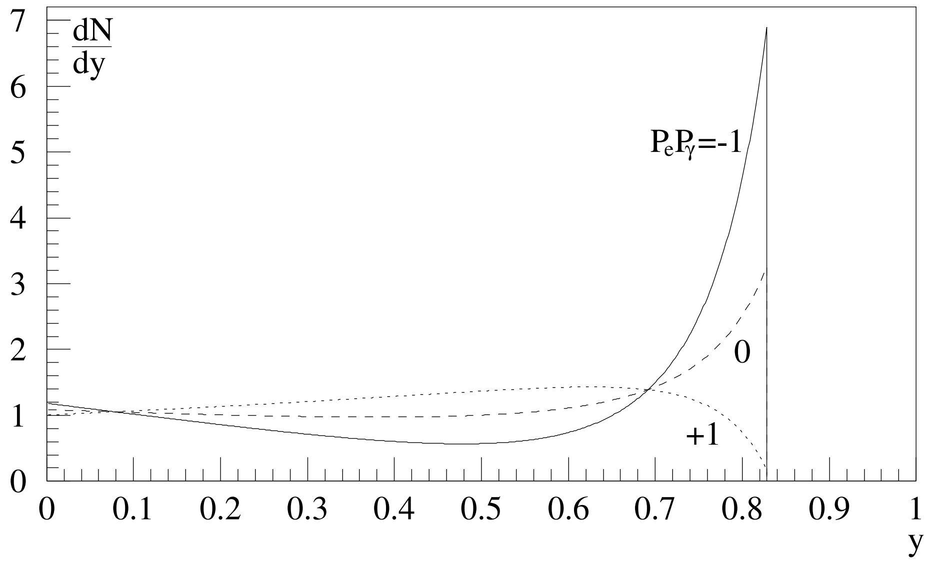

Figure 1: Energy spectrum of the backscattered photons for unpolarized beams, equal and opposite initial state helicities ($\omega_0 = 1.26\,\mathrm{eV}, E = 250\,\mathrm{GeV}$).

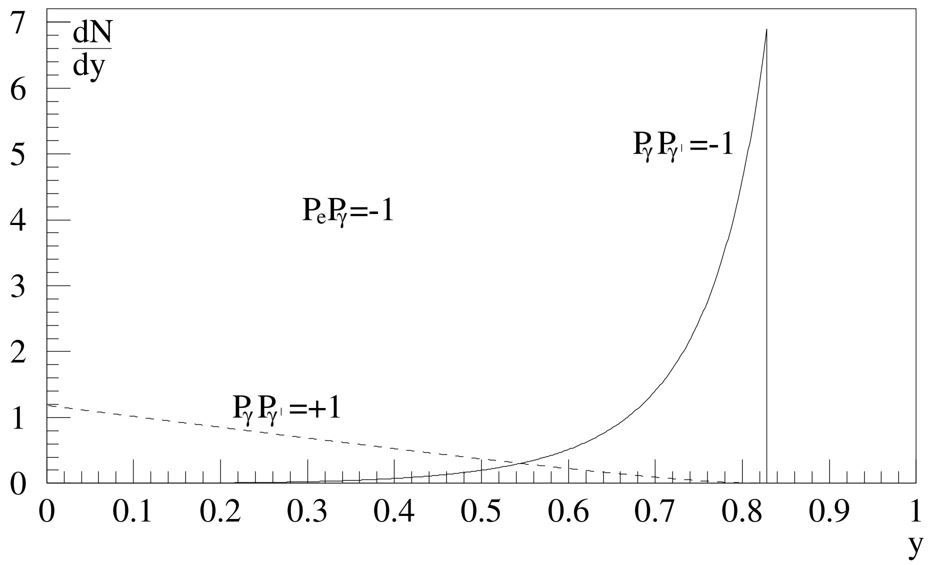

Figure 2: Energy spectrum of the backscatetred photons for opposite initial state helicities and helicity flipped (solid) respectively helicity conserved (dashed) final state ($\omega_0 = 1.26\,\mathrm{eV}, E = 250\,\mathrm{GeV}$).

The luminosity depends on the helicities of incoming as well as outgoing particles. Since all $\gamma\gamma$ reactions of interest are dependent on the helicities of the photons it is mandatory to decompose dL/dz according to helicity components. The fraction of e^+e^- cms energy transformed to $\gamma\gamma$ cms energy is denoted by z. The differential luminosities can be calculated in closed analytical form:

$$\begin{aligned}
\frac{dL}{dz} &= \frac{z}{(\sigma_c^{np} + P_e P_\gamma \sigma_c^p)(\sigma_c^{np} + \tilde{P}_e \tilde{P}_\gamma \sigma_c^p)} \Big[\Phi_1 + \left(P_e P_\gamma + \tilde{P}_e \tilde{P}_\gamma\right) \Phi_2 \\
&\quad + P_e P_\gamma \tilde{P}_e \tilde{P}_\gamma \Phi_3 + \left(P_e P_{\gamma'} + \tilde{P}_e \tilde{P}_{\gamma'}\right) \Phi_4 + \left(P_\gamma P_{\gamma'} + \tilde{P}_\gamma \tilde{P}_{\gamma'}\right) \Phi_5 \\
&\quad + P_e \tilde{P}_e \left(P_\gamma \tilde{P}_{\gamma'} + P_{\gamma'} \tilde{P}_\gamma\right) \Phi_6 + P_\gamma \tilde{P}_\gamma \left(P_e \tilde{P}_{\gamma'} + P_{\gamma'} \tilde{P}_e\right) \Phi_7 \\
&\quad + P_{\gamma'} \tilde{P}_{\gamma'} \left(P_e \tilde{P}_\gamma + P_\gamma \tilde{P}_e\right) \Phi_8 + P_e P_{\gamma'} \tilde{P}_e \tilde{P}_{\gamma'} \Phi_9 + P_\gamma P_{\gamma'} \tilde{P}_\gamma \tilde{P}_{\gamma'} \Phi_{10}\Big]
\end{aligned}$$

$$\sigma_c^{np} = \frac{1}{2} + \frac{8}{x} - \frac{1}{2\,(x+1)^2} + \left(1 - \frac{4}{x} - \frac{8}{x^2}\right) \ln\,(x+1)$$

$$\sigma_c^{p} = -\frac{5}{2} + \frac{1}{(x+1)} - \frac{1}{2\,(x+1)^2} + \left(1 + \frac{2}{x}\right) \ln\,(x+1)$$

The cross sections in this formula are normalized relative to $2\pi\alpha^2/xm_e^2$. The functions Φ_i are listed in the appendix. From the requirements of a luminosity peaked toward high energies it is ideal to choose for the incoming electrons and photons $P_e P_\gamma = \tilde{P}_e \tilde{P}_\gamma = -1$. The difference between unpolarized and fully polarized initial states is shown in Fig. 3 after summation over final state helicities. For the evaluation of the top quark pair production rate (like for any other reaction) it is interesting to distinguish between the four distributions corresponding different polarisations of the scattered photons. This decomposition is shown for ideal polarization in Fig. 4, where $h_{\gamma\gamma} = P_{\gamma'} - \tilde{P}_{\gamma'}$ denotes the total helicity of the photon-photon system. The case $h_{\gamma\gamma} = 0$ is appropriate for the production of ${}^1S_0$ toponium resonances so that $P_e = \tilde{P}_e$ and $P_\gamma = \tilde{P}_\gamma$ is a suitable choice for the incoming helicities. The contributions from $P_{\gamma'} = -1$, $\tilde{P}_{\gamma'} = 1$ and $P_{\gamma'} = 1$, $\tilde{P}_{\gamma'} = -1$ are identical and therefore added in one curve.

3 Top quark production rate

3.1 Born approximation

The Born cross section for the process $\gamma\gamma \to t\bar{t}$ is given by

$$\sigma^0_{\gamma\gamma\to t\bar{t}}\,(s) = \frac{\sigma_{++} + \sigma_{+-} + \sigma_{-+} + \sigma_{--}}{4} \tag{3}$$

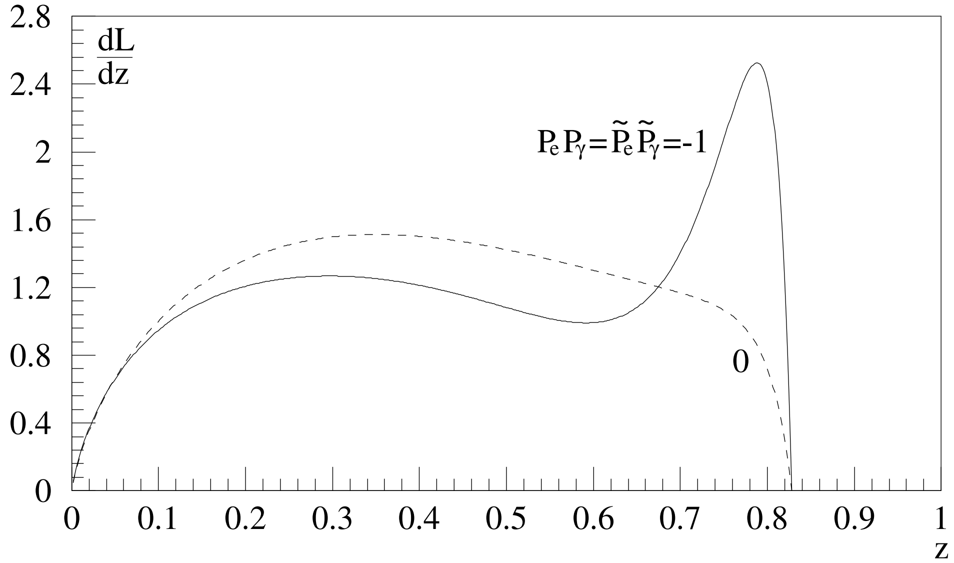

Figure 3: Spectral luminosity for $P_e = P_\gamma = \tilde{P}_e = \tilde{P}_\gamma = 0$ (dashed) and $P_e P_\gamma = \tilde{P}_e \tilde{P}_\gamma = -1$ (solid), ($\omega_0 = 1.26$ eV, E = 250 GeV).

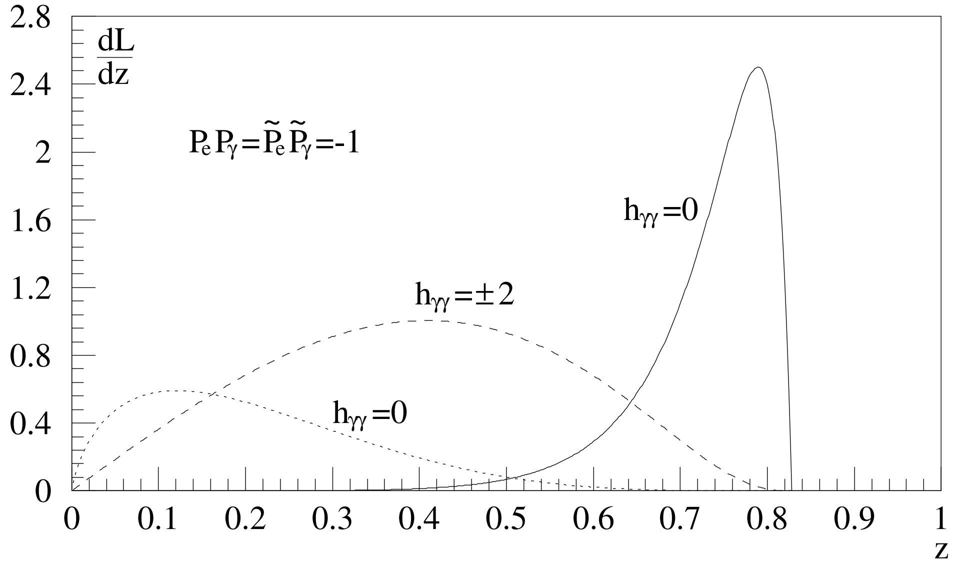

Figure 4: Spectral luminosity dependence on final state photon polarisation, ($\omega_0 = 1.26$ eV, E = 250 GeV).

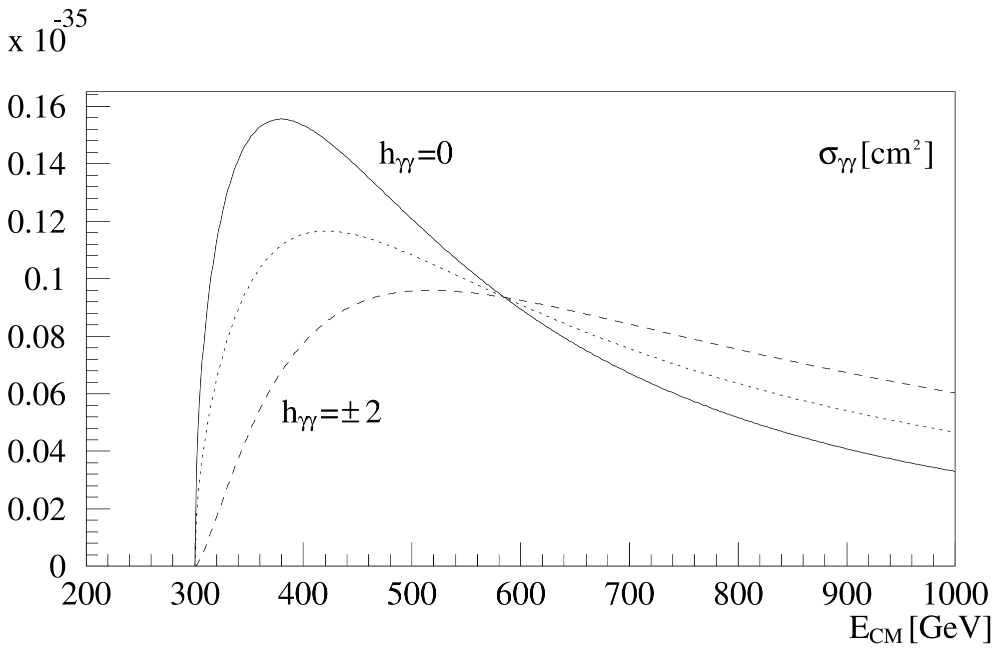

Figure 5: $\sigma^0_{\gamma\gamma\to t\bar{t}}$ for $m_t = 150\,GeV$ and equal photon helicities (solid), opposite photon helicities (dashed) and unpolarized photons (dotted).

where

$$\beta = \sqrt{1 - \frac{4m_t^2}{s}}$$

$$\sigma_{++} = \sigma_{--} = \frac{2\pi\beta\alpha^2 Q^4 N_c}{s}\left[2\left(1+\beta^2\right) + \frac{(1-\beta^4)}{\beta}\ln\left(\frac{1+\beta}{1-\beta}\right)\right]$$

$$\sigma_{+-} = \sigma_{-+} = \frac{2\pi\beta\alpha^2 Q^4 N_c}{s}\left[-10 + 2\beta^2 + \frac{5-\beta^4}{\beta}\ln\left(\frac{1+\beta}{1-\beta}\right)\right]$$

The number of colors is denoted by $N_c = 3$, the electric charge by $Q = 2/3$ and the plus and minus indices refer to the photon helicities ± 1. The cross sections for different photon helicities is shown in Fig. 5. To obtain the effective cross section for top pair production the $\gamma\gamma$ cross section is folded with the $\gamma\gamma$ luminosity:

$$\sigma^{eff}_{\gamma\gamma\to t\bar{t}}(s_{ee}) = \sum_{P_{\gamma'}\tilde{P}_{\gamma'}} \int_{\frac{2m_t}{\sqrt{s_{ee}}}}^{\frac{x}{x+1}} dz\, \frac{dL}{dz}\sigma_{\gamma\gamma\to t\bar{t}}(z^2 s_{ee})$$

The cross sections for different helicity configurations are weighted with the corresponding luminosities, i. e. σ_{++} and σ_{--} are multiplied with the two $h_{\gamma\gamma} = 0$ contributions and σ_{+-} and σ_{-+} with the $h_{\gamma\gamma} = \pm 2$ contributions of the luminosity. Whenever polarization of the incoming electron and photon is used to improve the luminosity this weighted summation has to be performed. The effective cross section is shown in Fig. 6. An appropriate choice of helicities enhances the effective cross section by more than a factor two. Close to the threshold the

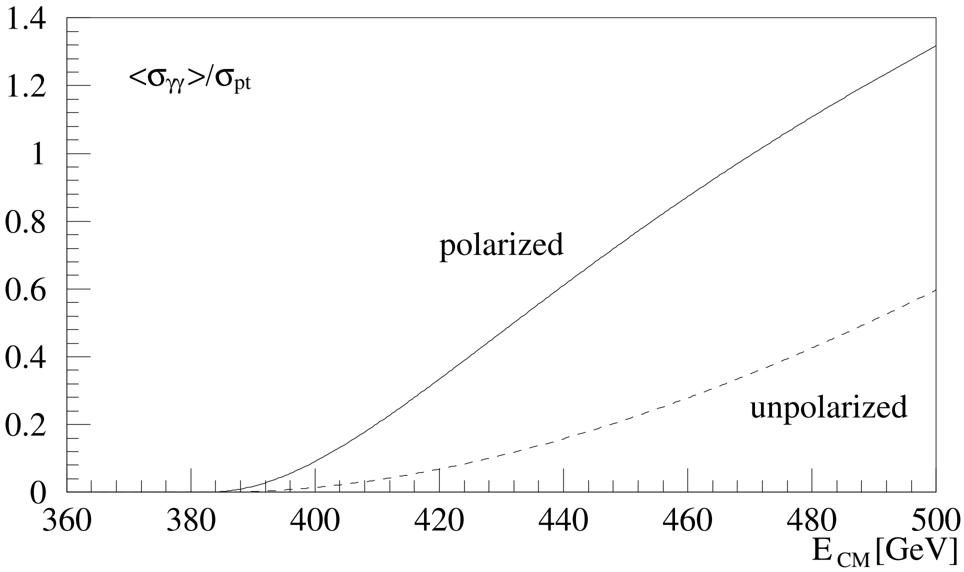

Figure 6: Effective cross section divided by $\sigma_{pt} = \dfrac{4\pi\alpha^2}{3s_{ee}}$, E_{CM} denotes the e^+e^- cms energy, ($m_t = 150$ GeV).

enhancement is even stronger since only the S-wave appears and the P-wave is strongly suppressed. This can be seen directly by expanding the matrix element in powers of β. The leading term of σ_{++} resp. σ_{--} is linear, the leading term of σ_{+-} resp. σ_{-+} however starts with β^3. In Fig. 7 this threshold region is expanded indicating a enhancement by an order of magnitude. Top pair production starts above an e^+e^- energy of about 380 GeV which corresponds to a maximal photon photon energy of about 300 GeV.

3.2 Resonance production

Top production close to threshold proceeds through $^1S_0$ toponium resonances. With increasing mass the probability for a top quark to decay weakly into $b + W$ before annihilating with $\bar{t}$ becomes more and more important. The final state consists of a b-quark jet plus two leptons or two light-quark jets, and a open top meson or baryon at rest which subsequently decays weakly. For a top mass above 100 GeV the single quark decay almost exclusively exhausts all other decay modes and raises the toponium width quickly to the GeV range [11]. Beyond 130 GeV the width becomes larger than the level spacing. The narrow spacing between the high radial excitations together with the large top decay width will lead to an apparent contribution to R that comes quite close to the QCD corrected parton value already within the resonance region. The resonance cross section for the process $\gamma\gamma \to {}^1S_0$ can be obtained numerically by solving the Schrödinger equation

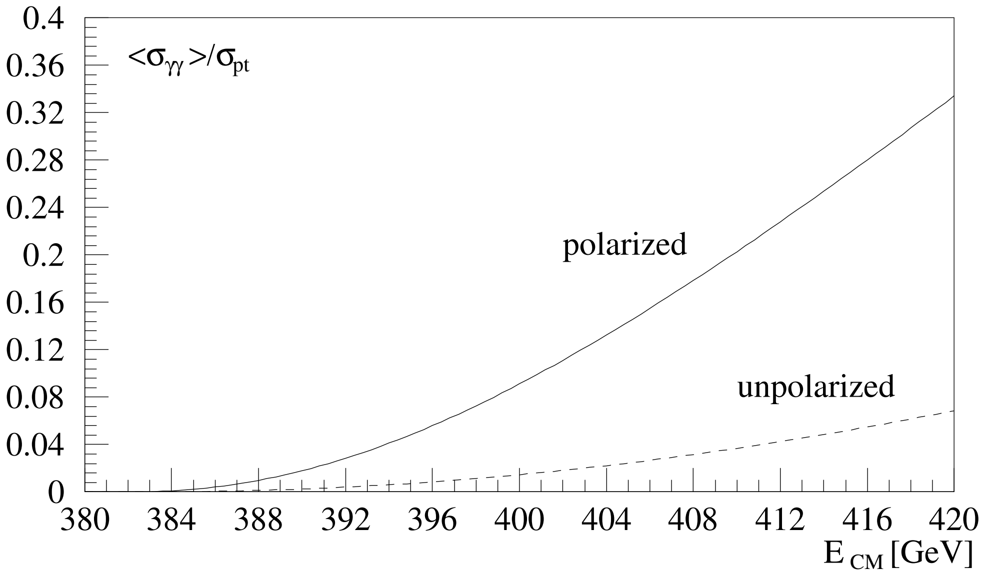

Figure 7: Effective cross section close above the threshold divided by $\sigma_{pt} = \dfrac{4\pi\alpha^2}{3s_{ee}}$, E_{CM} denotes the e^+e^- cms energy, ($m_t = 150$ GeV).

for the Greenfunction similary to the method proposed in [12, 13, 14] for e^+e^- annihilation or by summing Breit-Wigners (this is done earlier for $e^+e^- \to^3 S_1$ [15, 16]).The cross section $\sigma\left(\gamma\gamma \to^1 S_0\right)$ is related to $\sigma\left(e^+e^- \to^3 S_1\right)$ by applying the Breit-Wigner formula for both cases:

$$\sigma = \frac{\pi}{k^2}\frac{(2J+1)}{(2s_a+1)(2s_b+1)}\frac{\Gamma_i\Gamma_{tot}}{(E-M)^2+\Gamma_{tot}^2/4}$$

The $(2s+1)$ factors are the multiplicities of the initial spin states, to be replaced by 2 for unpolarized photons. k denotes the momentum of one of the initial state particles and hence $4k^2 = s$ for the cases of interest. The total toponium decay width assumed to be $2\Gamma(t \to b + W)$. The resonance mass M is approximately the same for ${}^3S_1$ and ${}^1S_0$ states. Γ_i denotes the decay width into the initial state. With an extra factor $\dfrac{1}{2}$ to account for identical particles in the final state one finds:

$$\frac{\sigma\left(\gamma\gamma \to^1 S_0\right)}{\sigma\left(e^+e^- \to {}^3S_1\right)} = \frac{2}{3}\frac{\Gamma\left({}^1S_0 \to \gamma\gamma\right)}{\Gamma\left({}^3S_1 \to e^+e^-\right)}$$

Using

$$\Gamma\left({}^1S_0 \to \gamma\gamma\right) = \frac{12Q^4\alpha^2|R(0)|^2}{M^2} \quad , \quad \Gamma\left({}^3S_1 \to e^+e^-\right) = \frac{4Q^2\alpha^2|R(0)|^2}{M^2}$$

one obtains for the ratio

$$\frac{\sigma\left(\gamma\gamma \to^1 S_0\right)}{\sigma\left(e^+e^- \to^3 S_1\right)} = 2Q^2 = \frac{8}{9}$$

This coincides with the ratio for open top production close to the threshold. Additional factors for the ratio between the two cross sections are induced by QCD corrections, to be considered in the following.

4 QCD corrections

4.1 Continuum cross section

In this section we calculate the complete order α_s QCD corrections to the cross section for $\gamma\gamma \to t\bar{t}$ production. The Born cross section $\sigma^0_{\gamma\gamma\to t\bar{t}}$ for open production vanishes at threshold (see eq. (3)) as a consequence of S-wave phase space suppression. The order α_s corrections are nececcary for a smoth matching between resonance and open flavor regions. Both the gluon bremsstrahlung amplitude squared and the interference between Born and one-loop graphs contribute in order α_s. The gluon bremsstrahlung cross section is given by the process

$$\gamma\,(k_1) + \gamma\,(k_2) \to g\,(k_3) + Q\,(p_1) + \overline{Q}\,(p_2)\,. \tag{4}$$

Six Feynman diagrams contributing to the amplitude.

Let us now briefly sketch some technical ingredients that go into our calculation. For the $O(\alpha_s)$ tree contributions in (4) we introduce the variables [17]

$$s = (k_1 + k_2)^2 \qquad t_1 = (k_2 - p_2)^2 - m_t^2 \qquad u_1 = (k_1 - p_2)^2 - m_t^2 \tag{5}$$

and $s_4 = (k_3 + p_1)^2 - m_t^2 = s + t_1 + u_1$. Averaging over the initial spins the cross section for the hard gluon bremsstrahlung can be written in the following form

$$\frac{d\sigma^H}{dt_1\,du_1} = \frac{\alpha_s \alpha^2}{8\pi s^2}\frac{s_4}{s_4 + m_t^2}\int_0^\pi d\theta_1 \sin\theta_1 \int_0^\pi d\theta_2\; R_{QED} \tag{6}$$

R_{QED} denotes the square of the matrix element of reaction (4) (without charges, color- and spin average factors). We checked that the square of the matrix element for hard radiation agrees with the expression found by Gunion and Kunszt [18]. The integration over the final state gluon is most easily performed in the quark-gluon CM system over the solid angle $d\Omega = \sin\theta_1 d\theta_1\, d\theta_2$ where θ_1 and θ_2 denote the polar and azimuthal angle of the gluon. In order to perform the angular integration in (6) we follow the procedure as outlined in [17]. Note that collinear divergences are absent in the tree contributions (4) as a consequence of the nonvanishing quark mass. The integration $d\Omega$ over the final state gluon is performed analytically and requires the evaluation of integrals of the following form

$$I^{(k,l)} = \int_0^\pi d\cos\theta_1 \int_0^\pi d\theta_2\; (a + b\cos\theta_1)^{-k}\,(A + B\cos\theta_1 + C\sin\theta_1\cos\theta_2)^{-l}\,, \tag{7}$$

where a, b, A, B and C are functions of the external kinematical variables s, t_1, u_1 and m_t^2 and k, l are positive ore negative integers. The neceassary sets of integrals can be found in [17]. Note that the reduction to this basic set of integrals is achieved only after very involved partial fractioning of the tree graph matrix elements.

Let us now turn to the virtual and soft contributions. The soft cross section is defined by the condition $0 \leq s_4 \leq \Delta$ in the bremsstrahlung diagrams of (4). The pole terms appearing in (4) originate from infrared singularities and cancel when the virtual and soft contributions are combined. For the sum of the virtual- and soft-gluon cross section σ^{V+S} we make use of the result of [17]. After average over the initial spins σ^{V+S} can be written as

$$\frac{d\sigma^{V+S}}{dt_1\, du_1} = \frac{2\alpha_s \alpha^2}{s^2} \delta\left(s + t_1 + u_1\right) \left[F^{V+S}_{QED}\left(t_1, u_1\right) + F^{V+S}_{QED}\left(u_1, t_1\right)\right] \tag{8}$$

where F^{V+S}_{QED} can be found in Appendix D of [17].

The remaining two dimensional integration in (6) and (8) are evaluated numerically. In our numerical program the $\ln^i(\Delta)$ (i=0,1) terms in σ^{V+S} were rewritten as integrals over s_4 [19]:

$$1 = \int_{\Delta}^{s_4^{max}} \frac{ds_4}{s_4^{max} - \Delta} \tag{9}$$

$$\ln \frac{\Delta}{m_t^2} = \int_{\Delta}^{s_4^{max}} \frac{s_4^{max}}{s_4^{max} - \Delta} \left[\ln \frac{s_4^{max}}{m_t^2} - \frac{s_4^{max} - \Delta}{s_4}\right] \tag{10}$$

In this way the virtual+soft piece and the hard piece can directly be added. The result is a flat s_4 distribution for the total order α_s correction σ^{V+S+H}. We checked that the total cross section is independent of Δ in the limit $\Delta \to 0$.

Near threshold the exact analytical behaviour can be extracted. The Taylor expansion in β of the correction factor is given by

$$\sigma_{\gamma\gamma\to t\bar{t}(g)} = \frac{12\pi\alpha^2 Q^4}{s}\beta \left[1 + \frac{4\alpha_s}{3\pi}\left\{\frac{\pi^2}{2\beta} - \left(5 - \frac{\pi^2}{4}\right) + O(\beta^1)\right\}\right] \tag{11}$$

It starts with an inverse power of β, familiar from Sommerfelds rescattering corrections. Combined with the phase space factor it leads to a step-function-like threshold behaviour. The next term in the expansion is identical to the correction factor for bound state production.

The cross section for open $t\bar{t}$ production can be cast into the form

$$\sigma_{\gamma\gamma\to t\bar{t}(g)} = \frac{\alpha^2 Q^4 N_c}{s}\left[f^{(0)}_{\gamma\gamma} + \frac{4}{3}\frac{\alpha_s}{\pi} f^{(1)}_{\gamma\gamma}\right] \tag{12}$$

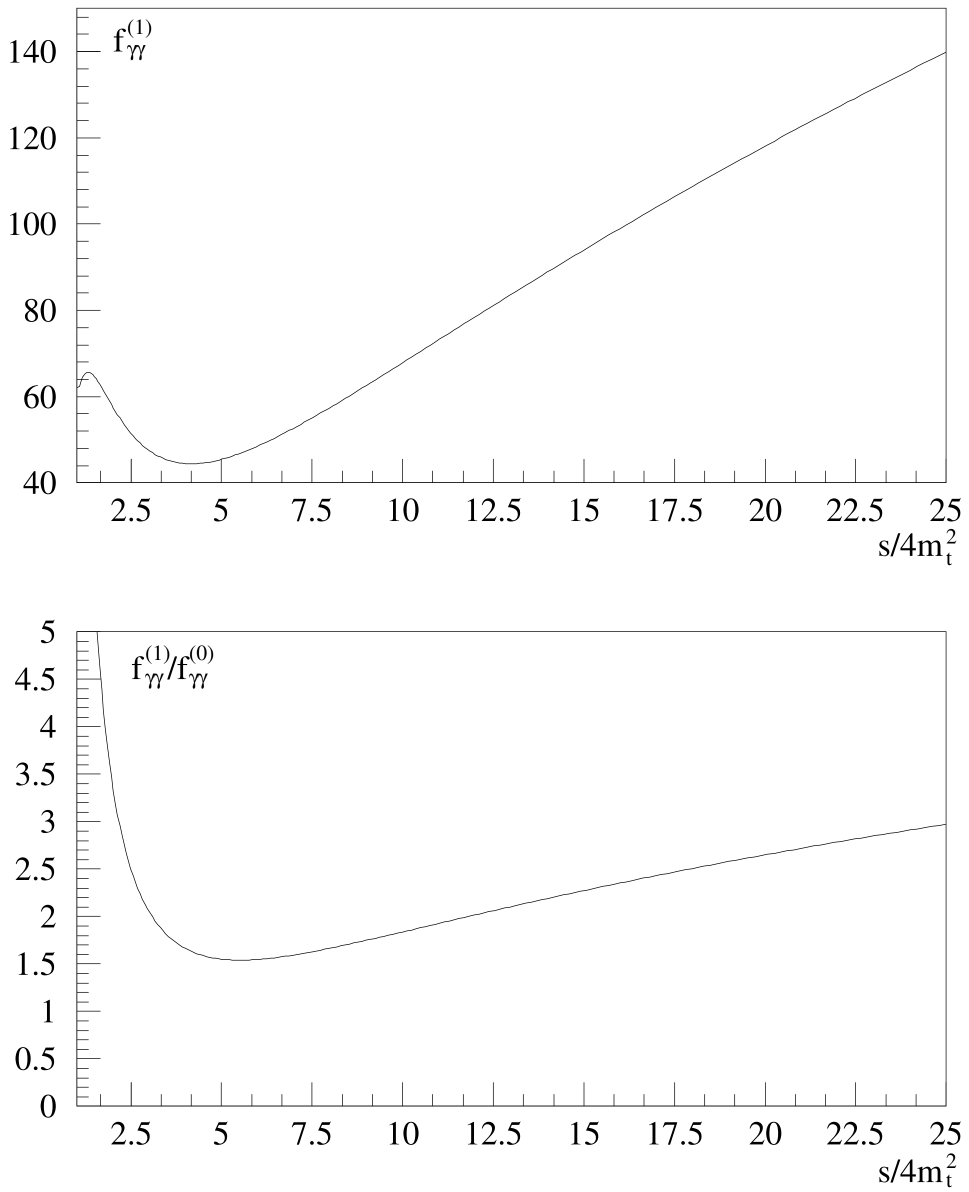

Figure 8: (a) Plot of $f_{\gamma\gamma}^{(1)}$ and (b) $f_{\gamma\gamma}^{(0)}/f_{\gamma\gamma}^{(0)}$ versus $s/4m_t^2$

$\frac{s}{4m_t^2}$	$f_{\gamma\gamma}^{(1)}$
1	62.009
4	44.489
9	62.613
16	98.998
25	139.89
100	339.96

Table 1: $f_{\gamma\gamma}^{(1)}$ for some values of $\frac{s}{4m_t^2}$.

where $f_{\gamma\gamma}^{(0)}$ and $f_{\gamma\gamma}^{(1)}$ depend on $\frac{s}{4m_t^2}$ only. A plot of $f_{\gamma\gamma}^{(1)}$ is shown in Fig. 8a. The ratio $f_{\gamma\gamma}^{(1)}/f_{\gamma\gamma}^{(0)}$ is shown in Fig. 8b. In Tab. 1 a set of characteristic results for $f_{\gamma\gamma}^{(1)}$ is displayed. These are in perfect agreement with those from Ref. [20].

4.2 Matching of reconances and continuum

Weak decays of densely spaced high radial excitationens of η_t lead to a form of the cross section below the threshold that is difficult to distinguish from continuum production in its shape and in the structure of the final state. Since QCD corrections are available for unpolarized photon beams only, the initial electron and laser beams are correspondingly considered to be unpolarized. The cross section with and without QCD corrections is shown in Fig. 11. QCD corrections enhance the effective cross sections by a large factor of about 40% in the region of interest. The resonance structures however, are completely smeared and do not show up in the total cross section. A fairly smooth transition between resonance and continuum region was obtained by adopting for the QCD corrections the two loop formula for $\alpha_{\overline{MS}}$, and a renormalization scale $\mu^2 = 4p^2$, similar to the matching condition for $t\bar{t}$ production in e^+e^- annihilation. We assumed $\Lambda_{\overline{MS}} = 200$ MeV. In Fig. 12 the effective differential mass distribution

$$\frac{d\sigma}{dz} = \frac{dL}{dz}\sigma\left(z^2 s\right)$$

is displayed for a ee center of mass energy of 500 GeV. Given high counting rates and a detector with sufficiently good mass resolution the resonant structures could be recovered.

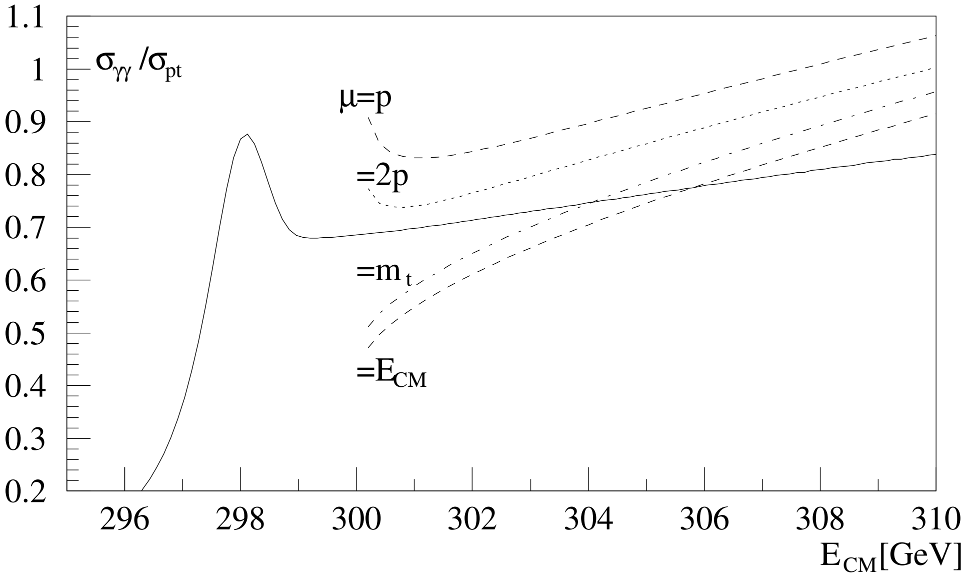

Figure 9: Matching between perturbative and bound state region with various renormalization scales and $m_t = 150$ GeV. The best matching in the intermediate region is obtained for $\mu = 2p$.

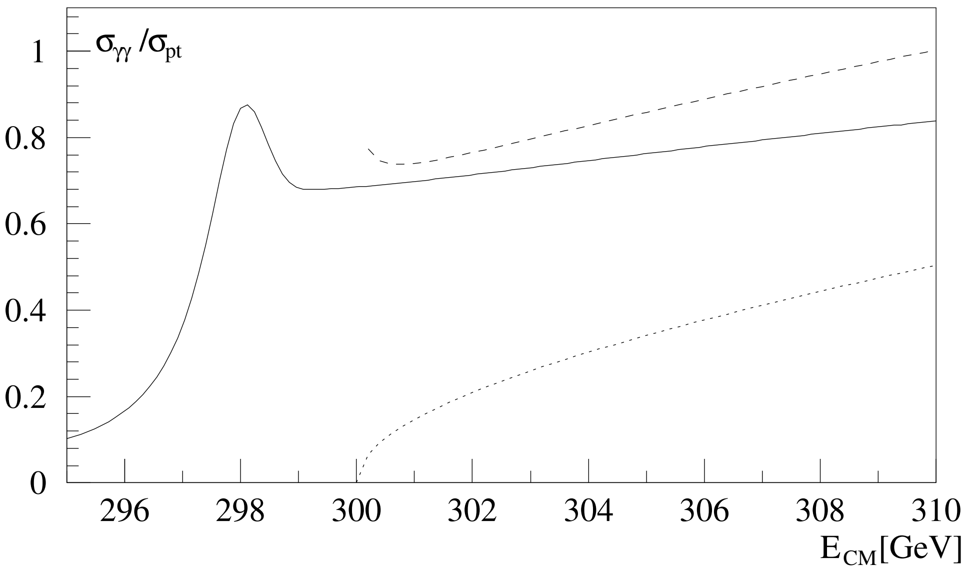

Figure 10: The cross section with and without QCD corrections, for $m_t = 150$ GeV and $\mu = 2p$.

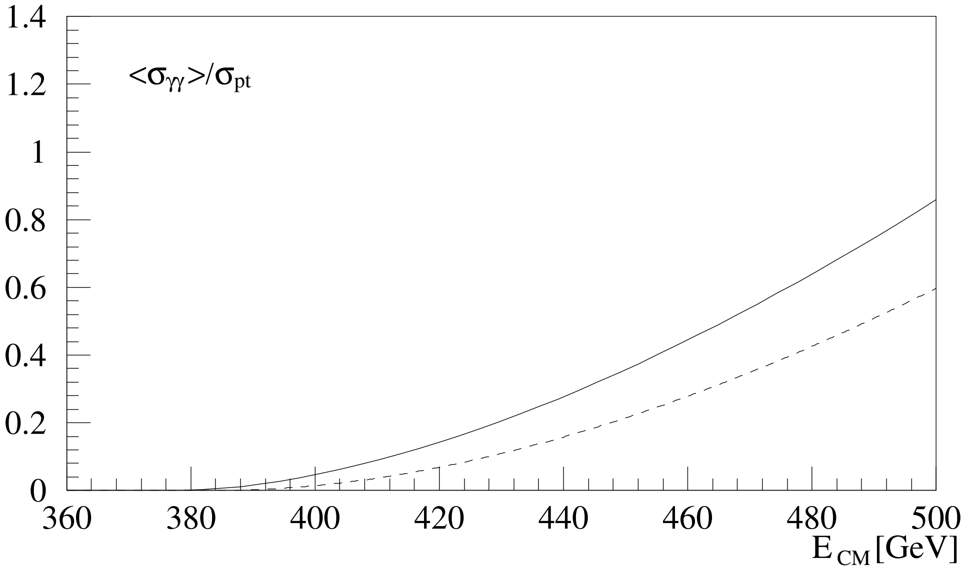

Figure 11: Effective cross section with (solid) and without (dashed) QCD corrections, ($\omega_0 = 1.26$ eV, $m_t = 150$ GeV and $\mu = 2p$).

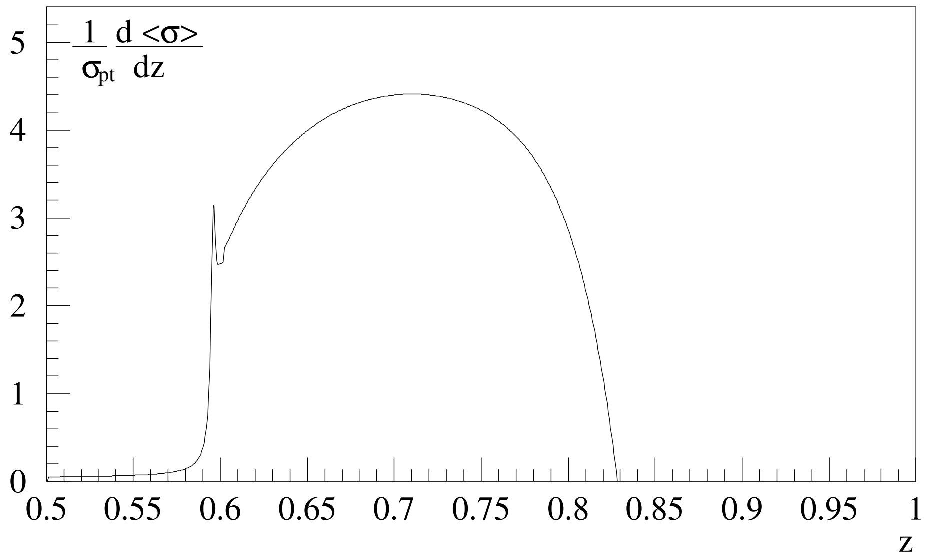

Figure 12: The effective differential mass distribution for a ee center of mass energy of 500 GeV

To summarize:
Top quark production at a Compton collider has been studied. The importance of providing polarized laser and electron beams has been stressed and the impact of this polarization on the production rate has been demonstrated. QCD corrections to the reaction without polarization have been calculated and found to be large.

Acknowledegement:
We thank M. Krämer, P. Zerwas and J. Zunft for discussions and for communicating us their results prior to publication and M. Jezabek and T. Teubner for providing the program for calculating the Greensfunction.

Appendix:
The functions Φ_i characterizing the differntial luminosities are given as follows.

$$\Phi_i = A_i A_0 + B_i \ln\left(\frac{x}{z\,(x+1)}\right) + C_i \ln\left(\frac{z}{x - z^2\,(x+1)}\right) \quad , \quad \zeta = \frac{1}{z^2-1}$$

$$\begin{aligned}
A_0 &= \frac{(z-x+xz)(z+x+xz)}{(x+1)(z^2-x+xz^2)} \\
A_1 &= 2\Big(\zeta^{-1} + \frac{1}{x}\left(1-\zeta^{-1}-2\zeta\right) - \frac{2}{x^2}\left(\zeta^{-1}-4-3\zeta\right) + \frac{8}{x^3}\zeta z^2\,(2+\zeta) \\
&\quad + \frac{8}{x^4}\zeta^2 z^4\Big) \\
A_2 &= \zeta - \frac{5}{x}\zeta z^2 + \frac{2}{x^2}z^2\left(2-5\zeta-4\zeta^2\right) + \frac{4}{x^3}z^2\left(1-\zeta-2\zeta^2\right) \\
A_3 &= -2\Big(\zeta^{-1} - \zeta + \frac{1}{x}z^2\left(3-\zeta-2\zeta^2\right) + \frac{2}{x^2}z^2\left(1-\zeta^2\right)\Big) \\
A_4 &= -\zeta^{-1} - \frac{1}{x}\left(5\zeta^{-1}+1+4\zeta\right) + \frac{4}{x^2}\,(5+3\zeta) \\
&\quad + \frac{4}{x^3}z^2\left(3+10\zeta+4\zeta^2\right) + \frac{8}{x^4}z^2\left(1+3\zeta+2\zeta^2\right) \\
A_5 &= (x+1)\left(\frac{1}{x}\left(3\zeta^{-1}+\zeta\right) - \frac{2}{x^2}\,(1+3\zeta) - \frac{4}{x^3}z^2\left(1+\zeta+2\zeta^2\right)\right) \\
A_6 &= -\,(x+1)\left(\frac{1}{x}\left(\zeta^{-1}-\zeta\right) + \frac{2}{x^2}z^2\,(1+3\zeta) + \frac{8}{x^3}\zeta^2 z^4\right) \\
A_7 &= -\zeta^{-1} + 2\zeta - \frac{1}{x}z^2\left(3-2\zeta-4\zeta^2\right) - \frac{2}{x^2}z^2\left(1-2\zeta^2\right) \\
A_8 &= -2\zeta^{-1} + \zeta - \frac{1}{x}\left(12\zeta^{-1}+9+5\zeta\right) - \frac{2}{x^2}\left(11\zeta^{-1}+14+11\zeta+4\zeta^2\right) \\
&\quad - \frac{4}{x^3}z^2\left(3+2\zeta+2\zeta^2\right)
\end{aligned}$$

$$
\begin{aligned}
A_9 &= 4\,(x+1)\,z^2\left(\frac{1}{x^2}\,(1-\zeta)+\frac{4}{x^3}\zeta z^2+\frac{4}{x^4}\zeta^2 z^4\right)\\
A_{10} &= 2\Big(2\zeta^{-1}+\zeta+\frac{1}{x}\left(6\zeta^{-1}+3+3\zeta+2\zeta^2\right)+\frac{2}{x^2}z^2\left(2+\zeta^2\right)\Big)
\end{aligned}
$$

$$
\begin{aligned}
B_1 &= 2\Big(1+\frac{2}{x}\left(\zeta^{-1}+3\right)+\frac{4}{x^2}\Big)\\
B_2 &= -\zeta^{-1}-2-\frac{2}{x}z^2-\frac{4}{x^2}z^2\\
B_3 &= 2z^2\Big(1+\frac{2}{x}\Big)\\
B_4 &= -\zeta^{-1}-2-\frac{2}{x}\left(\zeta^{-1}-1\right)-\frac{8}{x^2}\zeta^{-1}-\frac{8}{x^3}z^2\\
B_5 &= 2\Big(1+\frac{2}{x}\left(\zeta^{-1}+2\right)+\frac{2}{x^2}\left(\zeta^{-1}+2\right)\Big)\\
B_6 &= 2z^2\Big(1+\frac{3}{x}+\frac{2}{x^2}\Big)\\
B_7 &= -\zeta^{-1}-2-\frac{4}{x}z^2-\frac{4}{x^2}z^2\\
B_8 &= -\zeta^{-1}-2-\frac{4}{x}\zeta^{-1}-\frac{8}{x^2}\zeta^{-1}-\frac{8}{x^3}z^2\\
B_9 &= 2z^2\Big(1+\frac{4}{x}+\frac{4}{x^2}\Big)\\
B_{10} &= 2\Big(1+\frac{2}{x}z^2+\frac{4}{x^2}z^2\Big)
\end{aligned}
$$

$$
\begin{aligned}
C_1 &= \zeta^{-1}+\zeta-\frac{4}{x}\left(1+\zeta^{-1}+2\zeta\right)+\frac{8}{x^2}\left(2-\zeta^2\right)+\frac{32}{x^3}\zeta^2 z^4\\
&\quad+\frac{16}{x^4}\zeta z^2\left(1+3\zeta+2\zeta^2\right)\\
C_2 &= \zeta-\frac{2}{x}\zeta z^2\,(2-\zeta)+\frac{4}{x^2}z^2\left(1-\zeta-3\zeta^2\right)-\frac{16}{x^3}\zeta^3 z^4\\
C_3 &= -\zeta^{-1}+\zeta+\frac{4}{x}\zeta^2 z^2+\frac{4}{x^2}z^2\left(1+\zeta^2+2\zeta^3\right)\\
C_4 &= \zeta-\frac{2}{x}\left(\zeta^{-1}+3+4\zeta\right)+\frac{4}{x^2}\left(\zeta^{-1}+4-\zeta-2\zeta^2\right)\\
&\quad+\frac{8}{x^3}z^2\left(1+6\zeta+4\zeta^2\right)+\frac{32}{x^4}\zeta^3 z^6\\
C_5 &= \zeta^{-1}+\zeta-\frac{2}{x}\left(\zeta^{-1}+1+\zeta-\zeta^2\right)-\frac{4}{x^2}\left(\zeta^{-1}+1+4\zeta+3\zeta^2\right)-\frac{16}{x^3}\zeta^3 z^4\\
C_6 &= -\zeta^{-1}+\zeta-\frac{2}{x}\zeta z^2\,(2-\zeta)+\frac{4}{x^2}z^2\left(2-2\zeta-3\zeta^2\right)
\end{aligned}
$$

$$
\begin{aligned}
& +\frac{8}{x^3} z^2\left(1-3\zeta^2-2\zeta^3\right) \\
C_7 &= \zeta\Big(1+\frac{4}{x}\zeta z^2+\frac{4}{x^2}\zeta z^2(1+2\zeta)\Big) \\
C_8 &= \zeta-\frac{2}{x}\left(\zeta^{-1}+1+\zeta-\zeta^2\right)-\frac{4}{x^2}\left(\zeta^{-1}+1+5\zeta+3\zeta^2\right)-\frac{8}{x^3}\zeta^2 z^2(3+2\zeta) \\
C_9 &= -z^2\Big(1-\zeta+\frac{8}{x}\zeta-\frac{8}{x^2}\left(2-\zeta^2\right)-\frac{32}{x^3}\zeta^2 z^4-\frac{16}{x^4}\zeta z^2\left(1+3\zeta+2\zeta^2\right)\Big) \\
C_{10} &= \zeta^{-1}+\zeta+\frac{4}{x}\zeta^2 z^2-\frac{4}{x^2} z^2\left(1-\zeta^2-2\zeta^3\right)
\end{aligned}
$$

References

[1] J.H. Kühn and P.M. Zerwas, Heavy Flavours in High Energy Electron-Positron Collisions, to appear in the Review Volume on Heavy Flavours, eds. A.J. Buras and M. Lindner; World Scientific Publications Co, Singapore 1992.

[2] F. Richard, preprint LAL 91–62 (1991).

[3] S.Y. Choi and F. Schrempp, *Phys. Lett.* **B 227** (1991) 149

[4] W. Bernreuther et al., Conv: J.H. Kühn; Top Quark Physics, Theoretical Aspects, TTP92-19.

[5] V.I. Telnov, Gamma-Gamma and Gamma-Electron Beams at Linear Colliders, Proc. of the Workshop on physics with Linear Colliders, Saariselkä, Finland, 1991.

[6] C. Akerlof, preprint UM HE 81–59 (1981).

[7] I.F. Ginzburg et al, *Nucl. Inst. Meth.* **205** (1983) 47.

[8] V.I. Telnov, *Nucl. Inst. Meth.* **A 294** (1990) 72.

[9] I.F. Ginzburg et al, *Nucl. Inst. Meth.* **219** (1984) 5.

[10] D.A. Bauer, D.L. Borden, D.O. Caldwell, preprint SLAC–PUB–5715 (1992)

[11] J.H. Kühn, P.M. Zerwas, *Phys. Reports* **167** (1988) 321

[12] V.S. Fadin, V.A. Khoze, *Sov. J. Nucl. Phys.* **48** (1988) 309

[13] M.E. Peskin, M.J. Strassler, *Phys. Rev.* **D 43** (1991) 1500

[14] M. Jeżabek, J.H. Kühn, T. Teubner preprint TTP 92–16
T. Teubner, Diploma thesis

[15] S. Güsken, J.H. Kühn, P.M. Zerwas, *Phys. Lett.* **B 155** (1985) 185

[16] W. Kwong, *Phys. Rev.* **D 43** (1991) 1488

[17] W. Beenakker, H. Kuijf, W.L. van Neerven, J. Smith, *Phys. Rev.* **D 40** (1989) 54

[18] J.F. Gunion, Z. Kunszt, *Phys. Lett.* **B 178** (1986) 296

[19] W. Beenakker et al., *Nucl. Phys.* **B 351** (1991) 507

[20] M. Krämer, P.M. Zerwas and J. Zunft, private communication.